

Interphase Engineering of $\text{LiNi}_{0.88}\text{Mn}_{0.06}\text{Co}_{0.06}\text{O}_2$ Cathodes Using Octadecyl Phosphonic Acid Coupling Agents

Harald Norrud Pollen, Inger-Emma Nylund, Øystein Dahl, Ann Mari Svensson, Daniel Brandell, Reza Younesi, Julian Richard Tolchard, and Nils Peter Wagner*



Cite This: *ACS Appl. Energy Mater.* 2023, 6, 12032–12042



Read Online

ACCESS |



Metrics & More



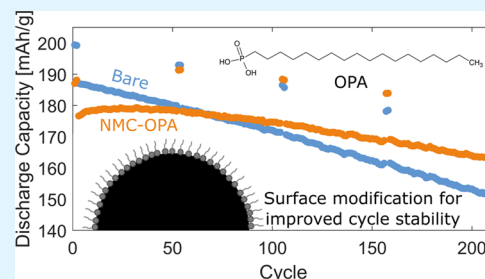
Article Recommendations



Supporting Information

ABSTRACT: Ni-rich layered oxides are proven high-energy cathode materials for Li-ion batteries, but their characteristic short cycle life remains a challenge for implementation on a wider scale. The surface reactivity of Ni-rich layered oxides is the driving force for several capacity fading mechanisms, and a common strategy to combat these issues is to apply a protective surface coating. In this work, $\text{LiNi}_{0.88}\text{Mn}_{0.06}\text{Co}_{0.06}\text{O}_2$ (NMC) is surface-modified using octadecyl phosphonic acid (OPA) as a coupling agent through a wet-chemical process. Post-treatments of the coated NMC material at 350 and 450 °C in an O_2 atmosphere are also evaluated. Physical characterization confirms the presence of a surface coating and confirms that the surface modification processing has a negligible effect on the bulk material structure. The bare NMC material shows an initial discharge capacity of 199 mAh/g in NMC||LTO cells. The coated NMC material shows a slightly lower initial discharge capacity of 188 mAh/g, but the capacity retention after 210 cycles improves from 86 to 95%. The coated NMC material shows higher discharge capacities than the bare NMC material beyond cycle 75. Postmortem characterizations indicate that the surface reactivity is reduced by the OPA coating as less fluorinated byproducts are formed. The high-temperature post-treatments of the coated NMC material change the surface chemistry but do not improve the electrochemical performance.

KEYWORDS: Ni-rich layered oxides, surface modification, post-treatment, octadecyl phosphonic acid (OPA), cathode electrolyte interphase (CEI), X-ray photoelectron spectroscopy (XPS), transmission electron microscopy (TEM)



INTRODUCTION

Ni-rich layered oxides ($\text{LiNi}_x\text{M}_{1-x}\text{O}_2$, $x > 0.5$, M = Mn, Co, Al) constitute a category of high-energy cathode materials for Li-ion batteries, which are technologically and commercially mature. The two main subclasses are $\text{LiNi}_x\text{Mn}_y\text{Co}_z\text{O}_2$ (NMC) and $\text{LiNi}_x\text{Co}_y\text{Al}_z\text{O}_2$ (NCA), and they are the dominating cathode materials in the electric vehicle market.¹ These materials acquire their high-energy densities from their high reversible capacities of 200 mAh/g delivered at ~4 V vs Li/Li⁺^{2,3,23} and they exhibit higher practical capacities compared to other commercial cathode materials, such as LiCoO_2 (145 mAh/g), LiMn_2O_4 (120 mAh/g), and LiFePO_4 (165 mAh/g).^{3,4} In addition, the Ni-rich layered oxides have low Co contents. This is desirable to lower material costs and alleviate ethical concerns related to Co-mining.^{1,5} NMC and NCA materials can have varying amounts of Ni, which is the main electrochemically active element of the transition metals in the cathode. A high Ni content is typically accompanied by a high capacity, still within a practically employed potential window. However, the cycle life and thermal stability decrease with increasing Ni content,^{6–8} resulting in a compromise between performance and stability. Ni-rich layered oxides, in which $x \geq 0.80$, have already been commercialized,^{9–11} but a large share of commercial NMC-based batteries still utilize lower Ni

contents.¹² While increasing the Ni fraction beyond 80 atom % is still desirable, the associated instabilities must be addressed further.

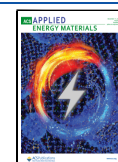
Ni-rich layered oxides adopt an $\alpha\text{-NaFeO}_2$ structure, isostructural to LiCoO_2 . The structure can be described based on a cubic close-packed oxygen lattice and with cations in all octahedral sites. The Li and TM (Ni, Mn, Co, Al) cations are ordered in alternating layers along the [111] cubic direction.^{13–15} The ordering creates a hexagonal distortion and a two-dimensional (2D) diffusion layer for the Li ions.^{16–18} In comparison, the cations in a rock-salt structure are randomly distributed.^{17,19} Layered oxides with high Ni contents are generally considered difficult to synthesize because they are sensitive to stoichiometric offsets and are prone to cation disordering. The cation ordering is driven by ionic size differences,^{14,20} but Li^+ and Ni^{2+} have similar ionic radii ($r(\text{Li}^+) = 0.76 \text{ \AA}$ and $r(\text{Ni}^{2+}) = 0.69 \text{ \AA}^{21}$), which causes a

Received: September 8, 2023

Revised: November 2, 2023

Accepted: November 17, 2023

Published: November 30, 2023



partial presence of Ni²⁺ in the Li layer. Optimization of the synthesis route is therefore essential to achieve a well-ordered Ni-rich layered oxide.^{14,20,22,23}

Ni-rich layered oxides exhibit reactive surfaces. Surface reconstruction in which the layered structure irreversibly transitions into spinel-type and rock-salt structures at the delithiated surface is one of the main capacity fading mechanisms for the associated batteries. The reconstruction involves the reduction of metastable Ni⁴⁺ to Ni²⁺ with an accompanied oxygen release from the lattice as charge compensation. Ni²⁺ can relocate to the Li layer, causing the layered structure to shift toward spinel- and rock-salt structures.^{7,19,23–26} The oxidative environment at the cathode surface also causes reactions between the organic electrolyte and cathode, creating a layer of decomposed electrolyte species on top of the active material. This layer is commonly termed the cathode electrolyte interphase (CEI). For electrolytes containing LiPF₆ and ethylene carbonate (EC), typically formed compounds include Li₂CO₃, Li₂O, LiF, MF_n (M = Ni, Mn, Co), ROCO₂Li, and Li_xPO_yF_z.^{7,27–29} Ni-rich layered oxides are also reactive toward H₂O and CO₂ when exposed to air, inducing the formation of LiOH and Li₂CO₃ surface impurities.^{30–32} Like other cathode materials, Ni-rich layered oxide surfaces are prone to transition metal dissolution from HF attack in LiPF₆-based electrolytes.³³ These parasitic reactions ultimately have a negative influence on electrochemical performance.

The repeated anisotropic volume changes experienced during (de)lithiation constitute another challenge for Ni-rich layered oxides, especially for polycrystalline materials. Most notable is the collapse of the layered structure along the *c*-axis, perpendicular to the Li and TM layers, at a highly delithiated state.^{34–37} The anisotropic volume changes can cause particle cracking, which allows the electrolyte to penetrate the particle. The fresh interior surface is exposed to the electrolyte, and further parasitic reactions may occur.^{7,27,35} Particle cracking can also cause active material loss by disconnecting particles from the conduction network within the electrode laminates.³⁸

The surface reactivity and oxygen release phenomena are important to control to achieve longevity. A common strategy is to coat the Ni-rich surface with a stable material, creating a protective barrier between the reactive surface and the electrolyte. The coating should be thin and uniform to not interfere with Li-transport or add extra dead weight while providing sufficient coverage. A wide variety of coating materials have been evaluated, including oxides such as Al₂O₃^{32,39} and TiO₂,³⁹ fluorides such as AlF₃,⁴⁰ and phosphates such as Li₃PO₄^{41–43} and MnPO₄.⁴⁴ These have been reported to be effective in improving Ni-rich layered oxides' electrochemical and thermal stabilities. Similarly, organo phosphonates,^{45,46} -phosphates,⁴⁷ -silane,⁴⁸ and -siloxanes³⁰ constitute an interesting group of coating materials because of their partly hydrophobic molecules, which can protect the Ni-rich surface against moisture and the formation of Li surface impurities.

In this work, in-house synthesized LiNi_{0.88}Mn_{0.06}Co_{0.06}O₂ (NMC) developed in our earlier work⁴⁹ is coated using octadecyl phosphonic acid (OPA) as a coupling agent through a wet-chemical route. The OPA molecule (Figure S1) has a –PO(OH)₂ functional group at the end of a linear hydrocarbon chain, with the added benefits of a hydrophobic tail and a functional group with a strong affinity to oxygen as P–O bonds are considered strong.⁴⁴ Modifications of the coated material

through post-treatments at 350 and 450 °C in an O₂ atmosphere are also explored to investigate if the electrochemical properties can be improved by, e.g., altering the hydrocarbon chain or the phosphonate functional group. The materials are investigated by physical characterization to understand the surface coating and to assess the impact of wet-chemical processing on the bulk material. Electrochemical characterization is used to evaluate the coatings' effect on the cycle life characteristics. Postmortem characterization is used to investigate possible capacity fading mechanisms.

EXPERIMENTAL SECTION

Synthesis of Polycrystalline LiNi_{0.88}Mn_{0.06}Co_{0.06}O₂ Bulk Material. Ni-rich layered oxide LiNi_{0.88}Mn_{0.06}Co_{0.06}O₂ (NMC) was synthesized through a single-pot oxalic acid coprecipitation route developed in earlier work.⁴⁹ In brief, LiNO₃ (99%, Alfa Aesar), Ni(CH₃COO)₂·4H₂O (≥98%, Alfa Aesar), Mn(CH₃COO)₂·4H₂O (≥99%, Merck), and Co(CH₃COO)₂·4H₂O (≥98%, Sigma-Aldrich) were used as precursors. Oxalic acid (C₂H₂O₄, 98%, Aldrich) was used as the precipitation medium, and HNO₃ (Sigma-Aldrich) and NH₃ (Merck) were used to adjust the pH. A solution with the Li, Ni, Mn, and Co precursors was prepared with a Li/(Ni + Mn + Co) molar ratio of 1.04, and the solution was adjusted to pH 3. The precursor solution was continuously fed into an oxalic acid solution adjusted to pH 3. The resulting suspension was aged for 19 h, and the solvent was evaporated. The dried precipitate was collected, ground, and calcined at 450 °C for 5 h in an air atmosphere to remove the organic compounds. The calcined powder was reground before a final heat treatment at 750 °C for 25 h in a tube furnace under a flowing O₂ atmosphere (12 NL/h). Lastly, the heat-treated powder was reground.

Surface Modification of LiNi_{0.88}Mn_{0.06}Co_{0.06}O₂ with Octadecyl Phosphonic Acid. The synthesized NMC was coated with an octadecyl phosphonic acid (OPA, C₁₈H₃₅O₃P) through a wet-chemical coating process employing isopropanol as a solvent. A 100 mL phosphonic solution was prepared by dissolving 0.2 g of OPA (97%, Sigma-Aldrich) in isopropanol. 3.8 g of NMC powder was dispersed in the phosphonic acid solution and stirred for 22 h at 25 °C. The NMC powder was collected by vacuum filtration, heat-treated at 140 °C in a vacuum furnace for 12 h, and gently ground. The treated NMC powder was further washed to remove nonreacted OPA material. The powder was first dispersed in 25 mL of isopropanol and sonicated for 15 min. The solvent was removed by centrifugation and decantation. The powder was redispersed with 25 mL of isopropanol and sonicated for another 15 min. The solvent was removed by filtration, and the remaining powder was rinsed with 50 mL of isopropanol. The powder was mortared and dried at 120 °C in a vacuum furnace. The resulting powder is referred to as NMC-OPA. For a fair comparison, the reference sample was prepared by running NMC through the same coating process without OPA to account for possible changes inflicted by the isopropanol processing. This reference sample is referred to as NMC-ISO.

2 g batches of NMC-OPA powder were further heat-treated at 350 and 450 °C, respectively, for 20 min in a tube furnace with a flowing O₂ atmosphere (6 NL/h). 200 °C/h heating and 300 °C/h cooling rates were used. The resulting powders are referred to as NMC-OPA-O350 and NMC-OPA-O450 based on their heat treatment temperature.

Physicochemical Characterization. X-ray diffraction (XRD) and Rietveld refinements were used to characterize the phase purities and crystal structures of the synthesized and modified NMC materials. Measurements were recorded on a Bruker D8 A25 DaVinci X-ray diffractometer with Mo–K_α radiation (λ = 0.71 Å), using a focusing Göbel mirror and equipped with a LynxEye XE 1D detector. The structural analyses via Rietveld refinements were similar as described in ref 49. In short, the refinements were based on an α-NaFeO₂ structure with an R3̄m space group with Li in the 3a position, M (Ni, Mn, Co) in the 3b position, and O in the 6c position. Li and Ni were allowed to switch positions. Peak shapes were modeled using a

fundamental parameters approach with microstrain-type peak broadening. The (003) reflection, usually included in NMC layered oxides, was omitted from the refinements due to the high degree of asymmetry in that reflection. It is noted that the shorter wavelength of Mo- K_{α} radiation versus Cu- K_{α} radiation ($\lambda = 1.54 \text{ \AA}$) allows for a larger number of reflections at low angles.

The particle morphologies were investigated by scanning electron microscopy (SEM) using an FEI Apreo SEM and a Hitachi SU9000 operating in secondary electron mode at 5.0 kV.

Thermogravimetric analysis (TGA) coupled with differential scanning calorimetry (DSC) performed on a Netzsch Jupiter STA449 instrument was used to investigate the thermal decomposition of bare and coated NMC materials. Approximately 20 mg of the materials was heated in alumina crucibles to 750 °C at 10 °C/min in an O₂ atmosphere flowing at 20 mL/min.

Surface-sensitive analyses were performed by X-ray photoelectron spectroscopy (XPS). Measurements were performed on a Kratos Axis Ultra with an electrostatic/magnetic hybrid lens and Al- K_{α} radiation ($E = 1486.6 \text{ eV}$) operating at 12 kV accelerating voltage and 10 mA emission current. Samples were mounted in a floating setup and electronically isolated from the sample holder. A charge neutralizer was implemented. Survey spectra were collected from 1200 to -5 eV with a 160 eV pass energy. Regional spectra, C 1s, O 1s, P 2p, and F 1s, were recorded with a 20 eV pass energy. Postmortem cathode samples were rinsed with dimethyl carbonate (DMC; $\geq 99\%$, Sigma-Aldrich), dried in an Ar glovebox, and transferred to the XPS instrument in an Ar-filled transfer chamber. XPS data sets were processed with CasaXPS software, with a Shirley background and adventitious carbon (C-C/C-H) calibrated to 284.8 eV. The data was not normalized during processing.

Postmortem transmission electron microscopy (TEM) analysis was performed on the cycled electrodes. The TEM cathode samples were rinsed similarly to the postmortem XPS samples. TEM lamellae were prepared using a focused ion beam (FIB; FEI Helios G4 UX). To avoid any damage to the area of interest, a protective carbon film was deposited by first using the electron beam for deposition and then using the ion beam. To ensure a high-quality surface on the lamellae, the final polishing step was performed using a 2 kV ion beam.

TEM investigations were performed on an aberration-corrected Jeol JEM ARM200F equipped with a cold field emission gun operated at 200 kV. Combined scanning transmission electron microscopy and electron energy-loss spectroscopy (STEM-EELS) was performed by using a beam semiconvergence angle of 27 mrad, and inner and outer collection angles of 119 and 471 mrad, respectively, for the high-angle angular dark-field (HAADF) STEM imaging. EELS spectra were acquired using a Quantum ER GIF for fast dual EELS with a collection angle of 67 mrad. The energy dispersion was 0.25 eV, and the step size was 4 Å. EELS quantification was performed by using Gatan DigitalMicrograph 3.4.3 with a Hartree-Slater cross section, a first order log-polynomial background model, and including edge overlap and plural scattering.

Electrochemical Characterization. Electrode sheets were fabricated by mixing 90 wt % NMC-based active materials, 5 wt % carbon black (CB; Imerys Super C65), and 5 wt % poly(vinylidene fluoride) (PVDF; Kynar HSV900) in *N*-methyl-2-pyrrolidone (NMP; Alfa Aesar) and homogenizing in a mixing mill (Retsch M3). The slurry was tape-cast onto Al foil using a 120 μm fixed gap applicator. The developed tapes were first dried in an oven at 80 °C for 45 min to remove most of the NMP solvent and subsequently kept at 120 °C to dry for 12 h in a vacuum oven. The cathode sheets were compressed by using a roller press (MTI Corporation, MSK-HRP-MR100A). Achieved cathode loadings were typically 4–5 mg_{NMC}/cm², corresponding to $\sim 1 \text{ mAh/cm}^2$ based on a 230 mAh/g first cycle capacity.

Overdimensioned NMC||LTO 2016 coin cells were assembled in a glovebox with an Ar atmosphere (MBraun, < 0.1 ppm of H₂O and < 0.1 ppm of O₂). 16 mm NMC-based cathode disks were combined with 18 mm LTO (Li₄Ti₅O₁₂; 2.0 mAh/cm²; CUSTOMCELLS) anode disks and 19 mm Celgard 2325 separators. 60 μL of 1 M LiPF₆ in ethylene carbonate and ethylene methylene carbonate (EC/EMC;

1:1 by volume; Sigma-Aldrich) was used as electrolyte. The cells were rested 24 h before electrochemical testing. Battery tests were conducted on a Lanhe CT2001A galvanostatic cycler. The cells were cycled between 1.5 and 2.8 V at 0.1 and 0.5C, where all currents were defined based on 1C being 180 mA/g. Equal charge and discharge rates were used. Constant current constant voltage (CCCV) charging processes were employed until the current had decayed to 0.1C. All cells were tested at 25 °C, and 2–4 cells were tested per cathode active material.

RESULTS AND DISCUSSION

The NMC and NMC-OPA pristine powders were investigated by TGA/DSC to determine the thermal decomposition of the OPA coating in an O₂ atmosphere and to assess the amount of coating material present on the sample. Figure 1 presents the

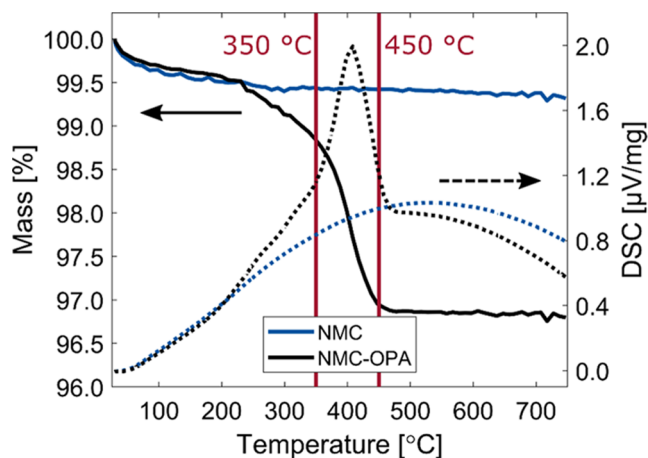


Figure 1. TGA/DSC measurements of NMC and NMC-OPA in an O₂ atmosphere upon heating. Solid lines show the mass losses, and dashed lines show the DSC signals. Red lines mark 350 and 450 °C.

mass loss and energy release upon heating as a function of temperature. Both samples show initial 0.3–0.4 wt % mass losses up to 100 °C, which are likely attributed to the release of H₂O and CO₂. The TGA/DSC signals of the materials start to deviate when heated above 230 °C, at which point an accelerated mass loss is observed for the coated NMC-OPA sample. The slope of the DSC signal suggests that the coated material has two distinct decomposition regions, 230–350 and 350–470 °C. A moderate mass loss of 0.7 wt % is detected in the first region, while a 2.0 wt % mass loss is observed in the second region. The exothermic peak is at 410 °C. The NMC-OPA mass loss above 230 °C is assigned to mass losses related to OPA.^{50–53} It is plausible that the mass loss at 230–350 °C is related to the loss of physisorbed OPA molecules, while the mass loss at 350–470 °C is associated with the burning of hydrocarbon chains of chemisorbed OPA molecules.

The bare NMC displays a 0.4 wt % continuous mass loss between 100 and 750 °C, likely due to instrument drift and the decomposition of surface impurities, such as LiOH and Li₂CO₃. The mass loss difference between NMC-OPA and NMC is 2.4 wt %, which also indicates the present coating amount. Compared to the 5.0 wt % added during the wet-chemical coating process, a significant portion thereby does not interact with the NMC material or is removed during the washing process. To elaborate on whether further heat treatment of the coating contributes to improved properties, two samples were prepared by post-treating NMC-OPA in an

O₂ atmosphere at 350 and 450 °C, i.e., temperatures below and above the steepest mass loss region, respectively.

The particle morphologies of the cathode active materials were investigated by SEM. The micrographs of the synthesized NMC material and the NMC-OPA-coated materials are displayed in Figure 2. The NMC particles have a polycrystal-

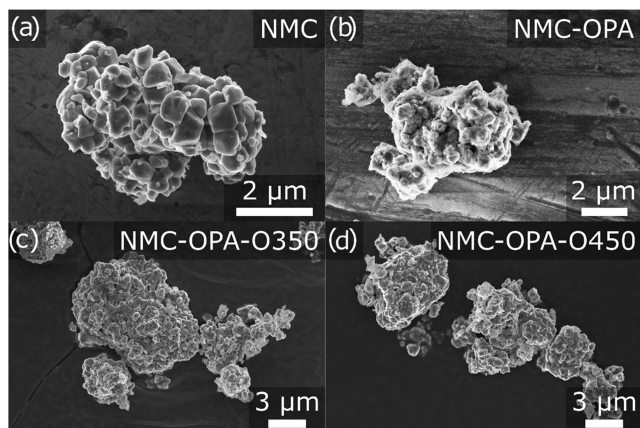


Figure 2. SEM micrographs of (a) NMC, (b) NMC-OPA, (c) NMC-OPA-O350, and (d) NMC-OPA-O450 pristine powder materials.

line morphology, consisting of submicron primary particles assembled into micron-sized secondary particles. The NMC-OPA particles show a similar primary and secondary particle morphology, but a surface modification is detected, indicating that OPA has then been deposited onto the NMC particles. The coating appears rough and porous, which could be

attributed to the long C₁₈ hydrocarbon chain of the OPA molecule. Surface layers are also present after the additional heat treatment (Figure 2c,d), but they appear to be more compact than the surface layer of NMC-OPA. This suggests that post-treatments affect the OPA coating.

XRD and Rietveld analyses were used to investigate the effect of the coating procedure on the bulk average Ni-rich layered oxide structure. The measured and calculated diffractograms of bare and coated NMC powder materials are displayed in Figure S2, and the calculated structural values are presented in Table S1. Overall, the structure does not change significantly during the coating process and post-treatments, which include isopropanol submersion and additional heat treatment up to 450 °C in an O₂ atmosphere. All of the prepared materials display diffraction patterns characteristic of the α-NaFeO₂ layered structure. No additional reflections are seen, demonstrating phase purity for the bare and surface-modified materials. The calculated unit cell parameters of the synthesized NMC material are $a = 2.8736 \text{ \AA}$ and $c = 14.1955 \text{ \AA}$ ($c/a = 4.940$), with 2.2 atom % Ni²⁺ in the Li layer.

The surface chemistries of the bare and coated NMC powder materials were characterized by XPS prior to electrode fabrication. The measured spectra and the suggested deconvoluted components are displayed in Figure 3, and the survey spectra in Figure S3. The binding energies of the deconvoluted components and their suggested species are listed in Table 1. The bare NMC and NMC-ISO materials show similar surface chemistries based on all O 1s, C 1s, and P 2p spectra. The C 1s and O 1s spectra indicate the presence of Li₂CO₃ surface impurities (~289 and ~531 eV) on the bare materials, a commonly observed impurity on Ni-rich layered

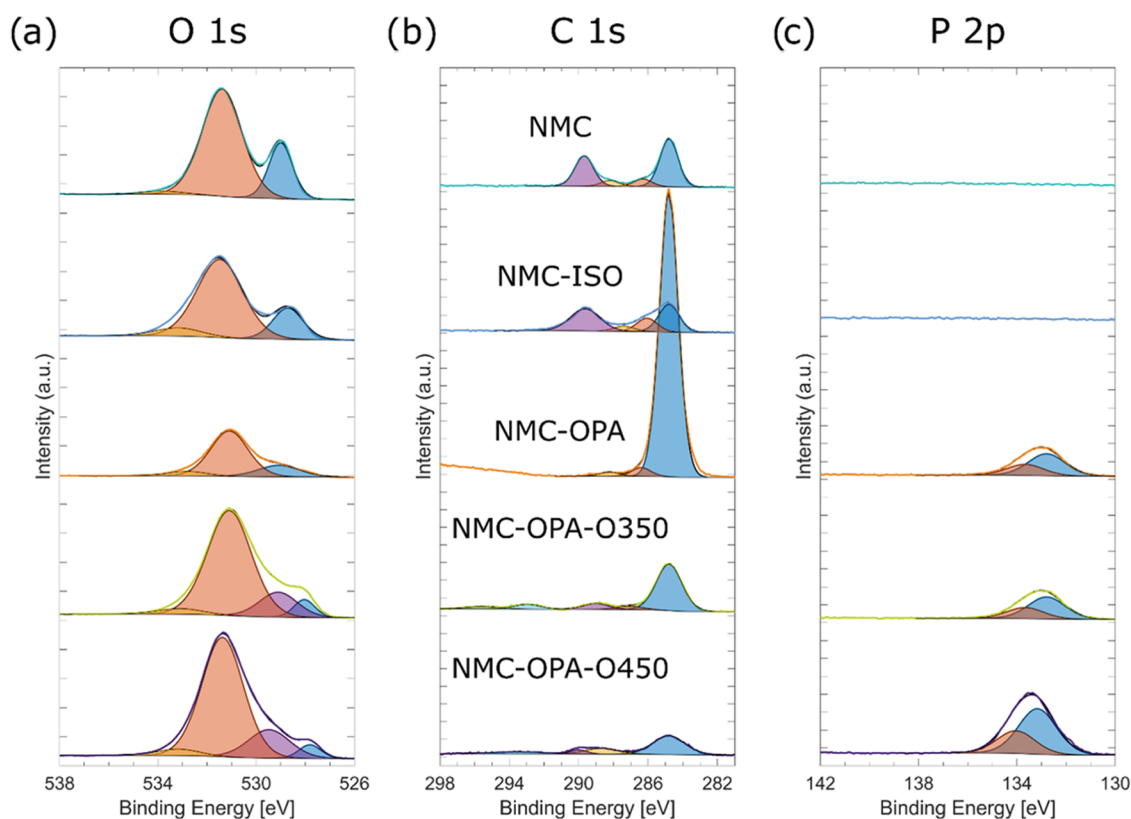


Figure 3. XPS (a) O 1s, (b) C 1s, and (c) P 2p regional spectra of pristine powder materials. Note that the spectra have not been normalized, and the vertical axes' intensity scales vary between the three panels.

Table 1. Deconvolution of XPS Data Collected from Pristine Powders with the Suggested Assigned Species^{a,3}

region	binding energy (eV)	assignment	based on reference
O 1s	~529 (blue/purple)	M–O (M = Li, Ni, Mn, Co)	29,54–57
	~531 (red)	C = O, CO ₃ ²⁻	29,54,56–58
	~533 (yellow)	P = O, PO ₄ ³⁻	54,58,59
		C–O–C/C–O	29,54,56–58
C 1s	284.8 (blue)	OH	60,61
	~286 (red)	P–O–P/P–O–M	59,62,63
	~288 (yellow)	C–C/C–H	60,64
	~289 (purple)	C–O–C/C–OH, C–O	29,56–58
P 2p	~289 (purple)	C = O, O–C–O	29,54,56–58,60
	~133 (blue/red)	O–C=O, CO ₃ ²⁻	56,57,60,64
		P–O/P = O, PO ₄ ³⁻	54,56,58,60,64

^aThe measured spectra with the corresponding deconvolutions are displayed in Figure 3.

oxide surfaces due to their reactivity toward H₂O and CO₂ when exposed to air.^{30,31}

All three coated materials show the presence of P–O/P = O bonded species (~133 eV) based on their P 2p spectra, a clear indication of a phosph(on)ate-type surface coating. In the O 1s spectra, the peaks related to lattice oxygen (~529 eV) and surface carbonate oxygen (~531 eV) are clearly split for the bare NMC materials, but the splitting is less evident for the three samples treated with OPA. This is expected since a coating is covering the Ni-rich oxide surface. For the post-treated materials, the variation in the lattice oxygen binding energy and the spectral weight around 530 eV may result from differential charging and possibly oxide defects. For the coated materials, there are contributions from P–O and P = O (~531 eV) in the O 1s spectra in addition to the oxygen surface impurities. The individual contributions from CO₃ and PO_x in the O 1s spectra cannot be resolved, but quantification of P 2p and deconvoluted C 1s spectra shows that the PO_x contribution is dominant in the coated samples.

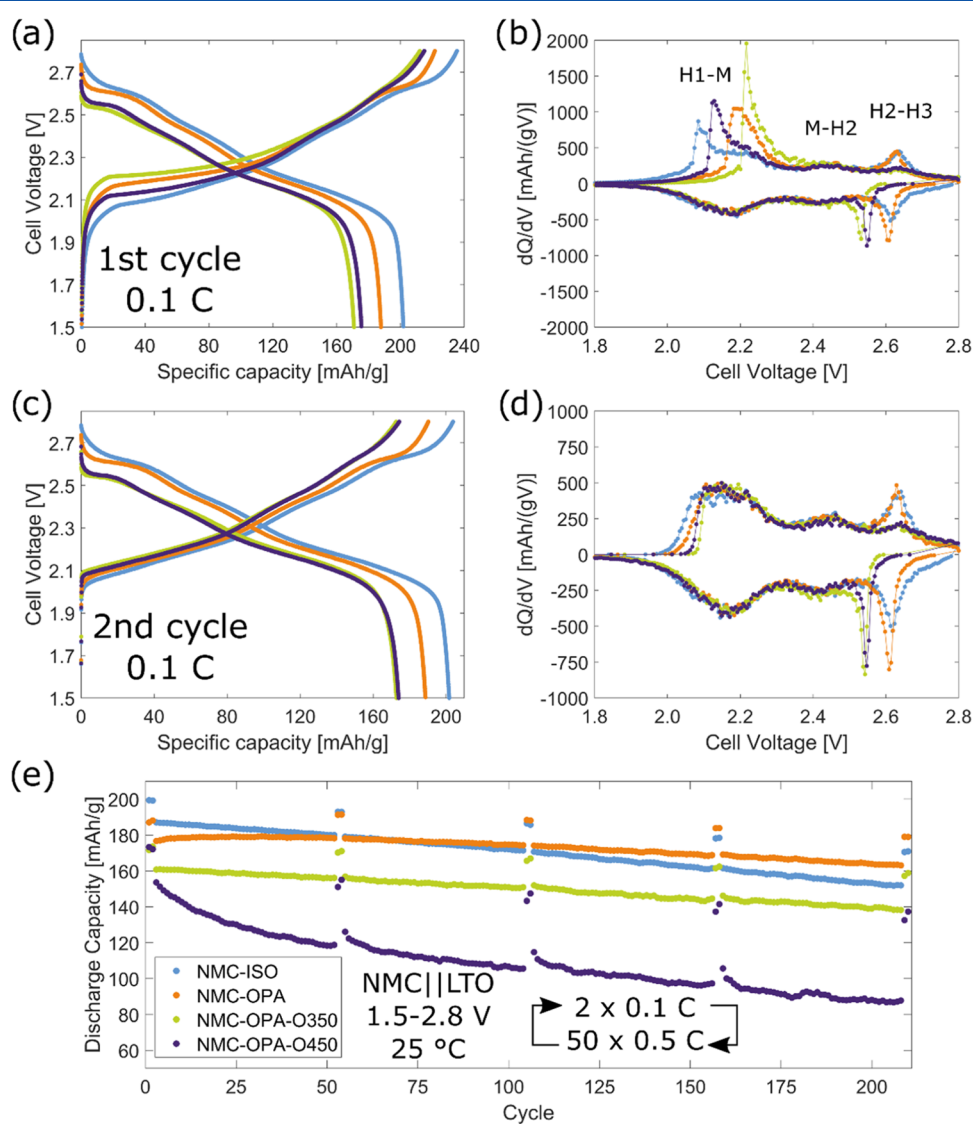


Figure 4. Electrochemical data from NMC||LTO full-cell testing. (a, c) Voltage profiles and (b, d) the corresponding differential capacity plots of the first and second cycles at 0.1C and (e) cycling test for 210 cycles. Cells were cycled between 1.5 and 2.8 V at 0.1 or 0.5C and 25 °C. The cycling test results are averaged values from 2 to 4 cells.

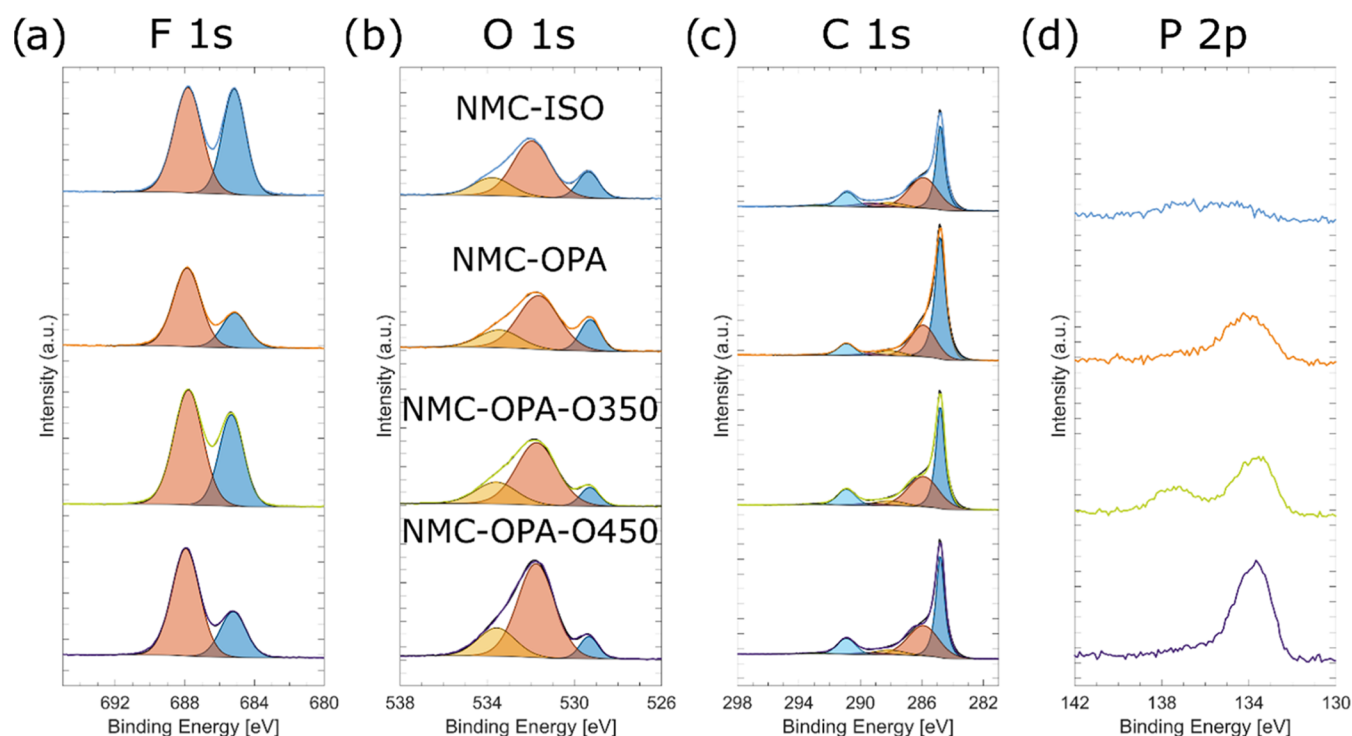


Figure 5. XPS (a) F 1s, (b) O 1s, (c) C 1s, and (d) P 2p regional spectra of postmortem cathodes cycled 54 times in NMC|LTO full-cell configuration, as reported in Figure S7. Note that the spectra have not been normalized, and the vertical axes' intensity scales vary between the four panels.

The C 1s spectrum of the coated NMC-OPA material is dominated by the hydrocarbon peak (284.8 eV), which is assigned to the long ($C_{18}H_{37}$) hydrocarbon chain of the OPA molecule. The intensity is significantly reduced relative to the oxidized carbon species when NMC-OPA is heat-treated at 350 and 450 °C, but the P 2p signal remains. Two additional low-intensity extra features are observed at ~ 293 and ~ 296 eV in the C 1s spectra for NMC-OPA heat-treated at 350 and 450 °C due to minor K impurities.

The XPS results of the pristine powders confirm the presence of an OPA coating and confirm that the coating is altered during the post-treatments. There is an apparent change in the organic chain of the OPA coating after post-treatment, and the results suggest that the long hydrocarbon chains decompose while leaving a phosphate-type surface layer. This is consistent with the observations reported by Chen et al., where an OPA-coated Al substrate was annealed in air up to 400 °C. They demonstrated that above 200 °C, the alkyl chains oxidize instead of the covalent P–O–Al bonds breaking.⁵¹ In this work, the O/P atomic ratio increases from ~ 3 for NMC-OPA to ~ 4.5 when heat-treated at 350 and 450 °C, respectively. This suggests that phosphonate ($-PO_3$) oxidizes to phosphate ($-PO_4$) during the two post-treatments.

To determine the effect of the coatings on the electrochemical properties, the materials were tested in NMC|LTO full cells. LTO was chosen as the anode material due to its high stability and the absence of SEI formation at its operating potential,^{29,65} thereby minimizing the possibility of the observed cell degradation originating from the anode. Figure 4a,b shows the first cycle potential profile and the accompanied differential capacity analysis when cycled between 1.5 and 2.8 V (3.0–4.3 V vs Li/Li⁺) at 0.1C and 25 °C. The achieved charge capacities and discharge capacities are presented in Table S2. The bare NMC-ISO achieves the highest capacities

with 233 mAh/g on charge and 199 mAh/g on discharge and the highest first cycle Coulombic efficiency (CE) at 85.7%. The coated NMC-OPA achieves 221 and 187 mAh/g during charge and discharge, respectively, with a CE close to the bare material. The NMC-OPA material thus shows a 6% lower discharge capacity than the bare NMC-ISO material, but 2.4 percentage points can be attributed to the amount of coating material, as found by TGA/DSC. The reversible capacities decrease further when NMC-OPA is heat-treated at 350 and 450 °C in an O₂ atmosphere. Both deliver 20 mAh/g less during charge and 25 mAh/g less during discharge compared with the bare NMC-ISO material. The accompanied CE values are reduced to $\sim 81\%$ for these two heat-treated samples.

Notably, all three coated samples show an increased polarization compared to the bare sample in the first cycle, as seen in Figure 4a,b. The increase in polarization is considerable for both post-treated samples while only marginal for the OPA-coated sample, suggesting the formation of an insulating surface film after the thermal decomposition of the OPA. This is reasonable, as the post-treatments do not significantly affect the bulk structures. Furthermore, the NMC-OPA samples post-treated at 350 and 450 °C show significantly lower average discharge voltages than NMC-ISO and NMC-OPA. The initial high polarization during charging of the coated samples is considerably lower from the second cycle (Figure 4c,d), but the lower discharge voltages remain. The increased polarization observed for the coated cathode materials is assigned to the extra (de)intercalation barrier created by the coating. The increased polarization for the post-treated samples is likely related to the densification of the surface layer, as observed by SEM. Both NMC-ISO and NMC-OPA show clear Ni-rich layered oxide potential profile features. During the charging process, there is a phase transition from a hexagonal (H1) to monoclinic (M) phase at ~ 2.1 V (~ 3.6 V

vs Li/Li⁺), followed by a transition to a second hexagonal phase (H2) at ~2.5 V (~4.0 V vs Li/Li⁺), and last to a third hexagonal phase (H3) at ~2.65 V (~4.15 V vs Li/Li⁺). These phase transitions agree with earlier reported observations,^{6,40,66} and the transition from H2 to H3 is associated with the lattice contraction along the *c*-axis.^{7,35,36,66} The NMC-OPA-O350 and NMC-OPA-O450 materials show weak and broad H2 to H3 transition peaks, which are shifted to higher charge voltages than the non-heat-treated materials. However, the corresponding H3 to H2 transitions are evident during subsequent discharge.

The cycle life characteristics were assessed through a 210-cycle test in the NMC||LTO full-cell configuration. These cells were cycled between 1.5 and 2.8 V at 25 °C and at alternating 0.1 and 0.5C currents. The results are presented in Figures 4e and S4. NMC-ISO shows the highest initial discharge capacities at both rates, delivering 199 mAh/g at 0.1 and 187 mAh/g at 0.5C, respectively. The capacity fade is slow and continuous, and the capacity retention is 86% at 0.1C and 81% at 0.5C after 210 cycles. NMC-OPA shows an ~10 mAh/g lower initial capacity at both rates than NMC-ISO. However, NMC-OPA shows a slight capacity increase over the first 50 cycles, and it delivers a higher capacity than NMC-ISO after 75 cycles. The capacity of NMC-OPA remains relatively stable beyond 75 cycles, and it retains 95% capacity at 0.1C and 92% at 0.5C after 210 cycles. The polarization growth is also low (Figure S4). NMC-OPA heat-treated at 350 °C shows an initial 0.1C capacity of 173 mAh/g. Although it retains 92% of its initial capacity at 0.1C, the reversible capacity is significantly lower compared to those of NMC-ISO and NMC-OPA. NMC-OPA heat-treated at 450 °C shows similar initial capacities to those of the sample heat-treated at 350 °C, but it fades considerably faster, losing 23% of its 0.5C capacity already after 52 cycles. The fade is less severe upon further cycling, and NMC-OPA-O450 displays a 78% retention at 0.1C and 57% at 0.5C after 210 cycling. The capacity difference between 0.1 and 0.5C is considerably higher compared to the other materials, indicating a poor rate performance. The CE of NMC-OPA-O450 is slightly lower compared to those of the other samples: 99.7% versus 99.8–99.9%. The CE values throughout the test are presented in Figure S5.

Though uncoated NMC-ISO shows the highest initial capacity, NMC-OPA performs best in terms of capacity retention. The layered oxide is coated with an amorphous OPA coating, which clearly contributes to improving the cycle life characteristics of the Ni-rich layered oxide. Further post-mortem characterizations were therefore conducted to investigate differences and possible degradation mechanisms of the various bare and coated samples.

Cathodes from NMC||LTO cells cycled 54 times were investigated by XPS. The measured F 1s, O 1s, C 1s, and P 2p regional spectra and the accompanying fitted features are shown in Figure 5, and the binding energies of the deconvoluted components and their suggested species are provided in Table 2. The survey spectra are displayed in Figure S6, and the cycling data of the cells from which the cathodes were extracted are shown in Figure S7. The postmortem measurements contain contributions from all components in the cathode laminate structure, including NMC active materials, CB, and PVDF binder. The C 1s spectra show similar characteristics for all of the samples, and the dominant hydrocarbon (284.8 eV) seen in the NMC-OPA pristine

Table 2. Deconvolution of XPS Data Collected from Postmortem Cathodes with the Suggested Assigned Species^a

region	binding energy (eV)	assignment	based on reference
F 1s	685.2 (blue)	LiF, MF _n	29,56–58,60,64
	687.8 (red)	C–F	29,56–58,60,64
O 1s	529.3 (blue)	M–O (M = Li, Ni, Mn, Co)	28,29,50,54–57
	531.7 (red)	C = O, CO ₃ ²⁻	29,54,56–58
		P = O, PO ₄ ³⁻	54,58,59
	533.5 (yellow)	C–O–C/C–O	29,54,56–58
C 1s	284.8 (blue)	OH	60,61
		P–O–P/P–O–M	59,62,63
	285.9 (red)	C–C/C–H	60,64
		C–O–C/C–OH, C–O	29,56–58
	288.1 (yellow)	CH ₂ –CF ₂	54,56–58
		C = O, O–C–O	29,54,56–58,60
	289.3 (purple)	O–C = O, CO ₃ ²⁻	56,57,60,64
	290.9 (sky blue)	CF ₂	56–58
	292.9 (green)	CF ₃	56–58
	P 2p	~134	P–O/P = O, PO ₄ ³⁻
~137		Li _x PO _y F _z , P–F	29,54,56,58

^aThe measured spectra with the corresponding deconvolutions are displayed in Figure 5. The cathodes were cycled 54 times in NMC||LTO full cells, with cycling data shown in Figure S7.

powder is no longer observed. The PVDF and CB cathode additives are probably substantial contributors to the C 1s spectra instead of the cathode active materials. For instance, the peaks at ~286, ~291, and ~293 eV are assigned CH₂–CF₂, CF₂, and CF₃, respectively, and are related to PVDF. The CB will also contribute to the hydrocarbon peak at 284.8 eV and the O–C–O/C = O peak at ~286 eV.⁵⁴

In the P 2p region, the coated samples show strong P–O/P=O signals (~134 eV) due to the phosph(on)ate bonds. This suggests that the coatings are still present after exposure to NMP solvent during electrode fabrication and after exposure to organic electrolyte in the battery cell. NMC-OPA-O350 has another distinct peak at ~137 eV, which is assigned to Li_xPO_yF_z, a CEI product formed by the decomposition of the LiPF₆ electrolyte salt. Slightly increased P 2p signals are observed for all samples, also attributed to Li_xPO_yF_z.

In the F 1s region, the ~688 eV peak is related to organic fluorine predominantly from PVDF. The peak at ~685 eV is related to LiF from LiPF₆ decomposition or MF_n transition metal fluorides formed from HF attack. The bare NMC-ISO cathode has a stronger LiF/MF_n signal than the coated samples, suggesting that there is less LiF formation on the coated samples and that the coatings provide protection against HF attack.

NMC-ISO and NMC-OPA cathodes were harvested from NMC||LTO full cells after 210 cycles and investigated for surface reconstruction layer buildup by TEM. These measurements were focused on particles at the electrode surface, and the results are presented in Figure 6. The selected area electron diffraction (SAED) measurements from the particle bulk (Figure 6c,d) confirm that the layered oxide structure is retained after cycling. The HAADF-STEM images (Figure 6e,f) show a clear layered structure at the bulk and out toward

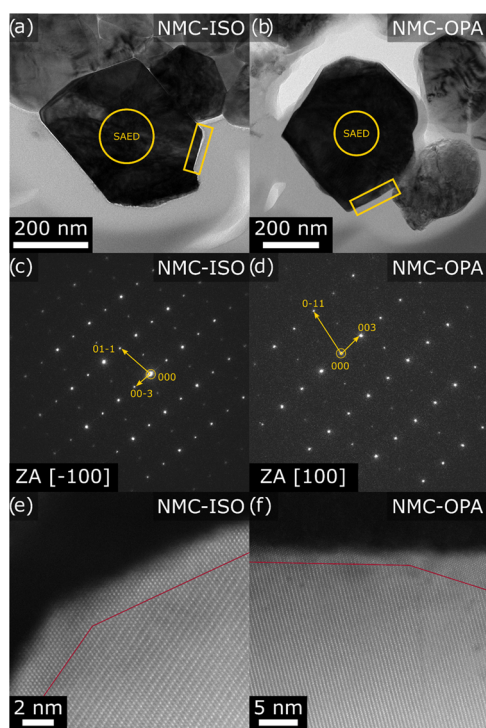


Figure 6. TEM data of (a, c, e) NMC-ISO and (b, d, f) NMC-OPA particles after 210 cycles in NMC||LTO full cells, as presented in Figure 4. (a, b) Bright-field TEM of particles, (c, d) SAED patterns of the bulk region, and (e, f) HAADF-STEM images of the surface region. The yellow rectangles (a, b) indicate the investigated surface regions. The red lines (e, f) mark the proximate boundary between the layered bulk structure and the surface reconstruction layer.

the surface, where the bright atomic columns indicate the TM layers of the structure.^{26,27,67} A clear surface reconstruction layer of ~2 to 5 nm is visible, where transition metals have entered the Li layers, forming a NiO-type structure. Based on the measured regions, both NMC-ISO and NMC-OPA cycled materials show approximately similar surface reconstruction layer thicknesses, implying that the surface modification does not inhibit rock-salt formation. The surface reconstruction layers observed here are relatively thin compared to other reported values in the literature.^{35,36,68–70} EELS measurements (Figure S8) reveal a Mn- and Co-enrichment at the surface compared to Ni for both NMC-ISO and NMC-OPA. The general trend for both materials is that the Ni and O concentrations increase the first few nanometers from the surface, while the Mn and Co concentrations decrease. Furthest away from the surface, the (Ni + Mn + Co)/O atomic ratio is 0.5, consistent with a stoichiometric layered oxide. This ratio increases toward the surface, as expected based on the surface reconstruction. The observed surface reconstruction is relatively thin after more than 200 cycles, contributing to small capacity fades for both materials.

Overall, the bare NMC-ISO material and the coated NMC-OPA material both had thin surface reconstruction layers after 210 cycles. The XPS surface chemistry investigation after 54 cycles suggests less LiF/MF_n CEI product buildup on the NMC-OPA material compared to the uncoated material, which is consistent with the low polarization growth. The OPA coating then protects and passivates the surface. The poor electrochemical performance of both post-treated materials is

likely related to an insulating film formed by the thermal decomposition of OPA.

CONCLUSIONS

Ni-rich NMC with 88 atom % Ni was coated using OPA as a coupling agent through a wet-chemical process and investigated by physical and electrochemical characterization. Physical characterization confirmed the presence of a coating layer and that the coating procedure did not affect the bulk layered structure to a significant degree. The OPA coating passivated the reactive NMC surface and improved the cycle life, although the initial capacity was slightly reduced compared to the bare sample. The coated NMC-OPA sample delivered an initial 188 mAh/g and a 95% capacity retention after 210 cycles in NMC||LTO full cells as compared to 199 mAh/g and an 86% capacity retention for the uncoated NMC. Postmortem investigations indicated that the OPA coating suppresses the surface parasitic reactions between the Ni-rich layered oxide surface and the electrolyte. Both coated and bare NMC formed equally thick surface reconstruction layers on both bare and OPA-coated NMC, but the coated material showed less formation of LiF and MF_n. Post-treatments of OPA-coated NMC at 350 and 450 °C in an O₂ atmosphere did not improve the electrochemical properties and induced increased polarization.

ASSOCIATED CONTENT

Supporting Information

The Supporting Information is available free of charge at <https://pubs.acs.org/doi/10.1021/acsaem.3c02275>.

Octadecyl phosphonic acid molecule; XRD and Rietveld refinement results; pristine and postmortem XPS survey spectra; initial capacities and Coulombic efficiencies for the NMC||LTO full cells; voltage profiles and Coulombic efficiencies cycling data for the NMC||LTO full cells; and postmortem EELS data (PDF)

AUTHOR INFORMATION

Corresponding Author

Nils Peter Wagner – Department of Materials Science and Engineering, NTNU Norwegian University of Science and Technology, 7491 Trondheim, Norway; Department of Sustainable Energy Technology, SINTEF Industry, 7491 Trondheim, Norway; orcid.org/0000-0002-8014-4324; Email: nils.p.wagner@ntnu.no

Authors

Harald Norrud Pollen – Department of Materials Science and Engineering, NTNU Norwegian University of Science and Technology, 7491 Trondheim, Norway

Inger-Emma Nylund – Department of Materials Science and Engineering, NTNU Norwegian University of Science and Technology, 7491 Trondheim, Norway

Oystein Dahl – Department of Sustainable Energy Technology, SINTEF Industry, 7491 Trondheim, Norway

Ann Mari Svensson – Department of Materials Science and Engineering, NTNU Norwegian University of Science and Technology, 7491 Trondheim, Norway

Daniel Brandell – Department of Chemistry—Ångström Laboratory, Uppsala University, SE-751 21 Uppsala, Sweden; orcid.org/0000-0002-8019-2801

Reza Younesi – Department of Chemistry—Ångström Laboratory, Uppsala University, SE-751 21 Uppsala, Sweden; orcid.org/0000-0003-2538-8104

Julian Richard Tolchard – Department of Sustainable Energy Technology, SINTEF Industry, 7491 Trondheim, Norway

Complete contact information is available at:
<https://pubs.acs.org/10.1021/acsaem.3c02275>

Notes

The authors declare no competing financial interest.

ACKNOWLEDGMENTS

The Research Council of Norway is acknowledged for financial support to the HiCath project (grant number 280910), support to the Norwegian Micro- and Nano-Fabrication Facility, NorFab (grant number 295864), and support to the Norwegian Center for Transmission Electron Microscopy, NORTEM (197405/F50). Parts of this work were performed within MoZEEs, a Norwegian Centre for Environment Friendly Energy Research (FME), co-sponsored by the Research Council of Norway (project number 257653) and 40 partners from research, industry, and the public sector. STandUP for Energy is also acknowledged.

REFERENCES

- (1) International Energy Agency (IEA) Global EV Outlook 2022: Securing Supplies for an Electric Future. In *Global EV Outlook 2022*; International Energy Agency: Paris, 2023.
- (2) Tarascon, J.-M.; Armand, M. Issues and Challenges Facing Rechargeable Lithium Batteries. *Nature* **2001**, *414*, 359–367.
- (3) Nitta, N.; Wu, F.; Lee, J. T.; Yushin, G. Li-Ion Battery Materials: Present and Future. *Mater. Today* **2015**, *18*, 252–264.
- (4) Julien, C. M.; Mauger, A.; Zaghib, K.; Groult, H. Comparative Issues of Cathode Materials for Li-Ion Batteries. *Inorganics* **2014**, *2*, 132–154.
- (5) Global Battery Alliance—World Economic Forum *A Vision for a Sustainable Battery Value Chain in 2030: Unlocking the Full Potential to Power Sustainable Development and Climate Change Mitigation*; Global Battery Alliance: Cologne/Geneva, 2019.
- (6) Noh, H.-J.; Youn, S.; Yoon, C. S.; Sun, Y.-K. Comparison of the Structural and Electrochemical Properties of Layered $\text{Li}[\text{Ni}_x\text{Co}_y\text{Mn}_z]\text{O}_2$ ($x = 1/3, 0.5, 0.6, 0.7, 0.8$ and 0.85) Cathode Material for Lithium-Ion Batteries. *J. Power Sources* **2013**, *233*, 121–130.
- (7) Sun, H.-H.; Manthiram, A. Impact of Microcrack Generation and Surface Degradation on a Nickel-Rich Layered $\text{Li}[\text{Ni}_{0.9}\text{Co}_{0.05}\text{Mn}_{0.05}]\text{O}_2$ Cathode for Lithium-Ion Batteries. *Chem. Mater.* **2017**, *29*, 8486–8493.
- (8) Lee, K.-S.; Myung, S.-T.; Amine, K.; Yashiro, H.; Sun, Y.-K. Structural and Electrochemical Properties of Layered $\text{Li}[\text{Ni}_{1-2x}\text{Co}_x\text{Mn}_x]\text{O}_2$ ($x = 0.1-0.3$) Positive Electrode Materials for Li-Ion Batteries. *J. Electrochem. Soc.* **2007**, *154*, A971–A977.
- (9) Schmuck, R.; Wagner, R.; Hörpel, G.; Placke, T.; Winter, M. Performance and Cost of Materials for Lithium-Based Rechargeable Automotive Batteries. *Nat. Energy* **2018**, *3*, 267–278.
- (10) Mikheenkova, A.; Gustafsson, O.; Misiewicz, C.; Brant, W. R.; Hahlin, M.; Lacey, M. J. Resolving High Potential Structural Deterioration in Ni-Rich Layered Cathode Materials for Lithium-Ion Batteries Operando. *J. Energy Storage* **2023**, *57*, No. 106211.
- (11) Li, W.; Erickson, E. M.; Manthiram, A. High-Nickel Layered Oxide Cathodes for Lithium-Based Automotive Batteries. *Nat. Energy* **2020**, *5*, 26–34.
- (12) Campagnol, N.; Erriquez, M.; Schwedhelm, D.; Wu, J.; Wu, T. Building Better Batteries: Insights on Chemistry and Design from China, 2023. <https://www.mckinsey.com/industries/automotive-and-assembly/our-insights/building-better-batteries-insights-on-chemistry-and-design-from-china>.

- (13) Hewston, T. A.; Chamberland, B. L. A Survey of First-Row Ternary Oxides LiMO_2 ($M = \text{Sc-Cu}$). *J. Phys. Chem. Solids* **1987**, *48*, 97–108.
- (14) Rougier, A.; Saadoune, I.; Gravereau, P.; Willmann, P.; Delmas, C. Effect of Cobalt Substitution on Cationic Distribution in $\text{LiNi}_{1-y}\text{Co}_y\text{O}_2$ Electrode Materials. *Solid State Ionics* **1996**, *90*, 83–90.
- (15) Bianchini, M.; Roca-Ayats, M.; Hartmann, P.; Brezesinski, T.; Janek, J. There and Back Again—The Journey of LiNiO_2 as a Cathode Active Material. *Angew. Chem., Int. Ed.* **2019**, *58*, 10434–10458.
- (16) Reimers, J. N.; Li, W.; Dahn, J. R. Short-Range Cation Ordering in $\text{Li}_x\text{Ni}_{2-x}\text{O}_2$. *Phys. Rev. B* **1993**, *47*, 8486–8493.
- (17) Bianchini, M.; Fauth, F.; Hartmann, P.; Brezesinski, T.; Janek, J. An In Situ Structural Study on the Synthesis and Decomposition of LiNiO_2 . *J. Mater. Chem. A* **2020**, *8*, 1808–1820.
- (18) Pickering, I. J.; Lewandowski, J. T.; Jacobson, A. J.; Goldstone, J. A. A Neutron Powder Diffraction Study of the Ordering in $\text{Li}_x\text{Ni}_{1-x}\text{O}$. *Solid State Ionics* **1992**, *53-56*, 405–412.
- (19) Hwang, S.; Chang, W.; Kim, S. M.; Su, D.; Kim, D. H.; Lee, J. Y.; Chung, K. Y.; Stach, E. A. Investigation of Changes in the Surface Structure of $\text{Li}_x\text{Ni}_{0.8}\text{Co}_{0.15}\text{Al}_{0.05}\text{O}_2$ Cathode Materials Induced by the Initial Charge. *Chem. Mater.* **2014**, *26*, 1084–1092.
- (20) Rougier, A.; Gravereau, P.; Delmas, C. Optimization of the Composition of the $\text{Li}_{1-z}\text{Ni}_{1+z}\text{O}_2$ Electrode Materials: Structural, Magnetic, and Electrochemical Studies. *J. Electrochem. Soc.* **1996**, *143*, 1168–1175.
- (21) Shannon, R. D. Revised Effective Ionic Radii and Systematic Studies of Interatomic Distances in Halides and Chalcogenides. *Acta Crystallogr., Sect. A: Cryst. Phys., Diffr., Theor. Gen. Crystallogr.* **1976**, *32*, 751–767.
- (22) Arai, H.; Okada, S.; Ohtsuka, H.; Ichimura, M.; Yamaki, J. Characterization and Cathode Performance of $\text{Li}_{1-x}\text{Ni}_{1+x}\text{O}_2$ Prepared with the Excess Lithium Method. *Solid State Ionics* **1995**, *80*, 261–269.
- (23) Hua, W.; Zhang, J.; Wang, S.; Cheng, Y.; Li, H.; Tseng, J.; Wu, Z.; Shen, C.-H.; Dolotko, O.; Liu, H.; Hung, S.-F.; Tang, W.; Li, M.; Knapp, M.; Ehrenberg, H.; Indris, S.; Guo, X. Long-Range Cationic Disorder Induces Two Distinct Degradation Pathways in Co-Free Ni-Rich Layered Cathodes. *Angew. Chem., Int. Ed.* **2023**, *62*, No. e202214880.
- (24) Lin, F.; Markus, I. M.; Nordlund, D.; Weng, T.-C.; Asta, M. D.; Xin, H. L.; Doeff, M. M. Surface Reconstruction and Chemical Evolution of Stoichiometric Layered Cathode Materials for Lithium-Ion Batteries. *Nat. Commun.* **2014**, *5*, No. 3529.
- (25) Abraham, D. P.; Twisten, R. D.; Balasubramanian, M.; Kropf, J.; Fischer, D.; McBreen, J.; Petrov, I.; Amine, K. Microscopy and Spectroscopy of Lithium Nickel Oxide-Based Particles Used in High Power Lithium-Ion Cells. *J. Electrochem. Soc.* **2003**, *150*, A1450–A1456.
- (26) Chen, J.; Yang, Y.; Tang, Y.; Wang, Y.; Li, H.; Xiao, X.; Wang, S.; Darma, M. S. D.; Etter, M.; Missyul, A.; Tayal, A.; Knapp, M.; Ehrenberg, H.; Indris, S.; Hua, W. Constructing a Thin Disordered Self-Protective Layer on the LiNiO_2 Primary Particles Against Oxygen Release. *Adv. Funct. Mater.* **2023**, *33*, No. 2211515.
- (27) Li, W.; Dolocan, A.; Oh, P.; Celio, H.; Park, S.; Cho, J.; Manthiram, A. Dynamic Behaviour of Interphases and Its Implication on High-Energy-Density Cathode Materials in Lithium-Ion Batteries. *Nat. Commun.* **2017**, *8*, No. 14589.
- (28) Edström, K.; Gustafsson, T.; Thomas, J. O. The Cathode-Electrolyte Interface in the Li-Ion Battery. *Electrochim. Acta* **2004**, *50*, 397–403.
- (29) Björklund, E.; Brandell, D.; Hahlin, M.; Edström, K.; Younesi, R. How the Negative Electrode Influences Interfacial and Electrochemical Properties of $\text{LiNi}_{1/3}\text{Co}_{1/3}\text{Mn}_{1/3}\text{O}_2$ Cathodes in Li-Ion Batteries. *J. Electrochem. Soc.* **2017**, *164*, A3054–A3059.
- (30) Doo, S. W.; Lee, S.; Kim, H.; Choi, J. H.; Lee, K. T. Hydrophobic Ni-Rich Layered Oxides as Cathode Materials for Lithium-Ion Batteries. *ACS Appl. Energy Mater.* **2019**, *2*, 6246–6253.
- (31) Hatsukade, T.; Schiele, A.; Hartmann, P.; Brezesinski, T.; Janek, J. Origin of Carbon Dioxide Evolved during Cycling of Nickel-Rich

Layered NCM Cathodes. *ACS Appl. Mater. Interfaces* **2018**, *10*, 38892–38899.

(32) Eom, J.; Kim, M. G.; Cho, J. Storage Characteristics of $\text{LiNi}_{0.8}\text{Co}_{0.1+x}\text{Mn}_{0.1-x}\text{O}_2$ ($x = 0, 0.03, \text{ and } 0.06$) Cathode Materials for Lithium Batteries. *J. Electrochem. Soc.* **2008**, *155*, A239–A245.

(33) Tesfamhret, Y.; Younesi, R.; Berg, E. J. Influence of Al_2O_3 Coatings on HF Induced Transition Metal Dissolution from Lithium-Ion Cathodes. *J. Electrochem. Soc.* **2022**, *169*, No. 010530.

(34) Li, W.; Asl, H. Y.; Xie, Q.; Manthiram, A. Collapse of $\text{LiNi}_{1-x-y}\text{Co}_x\text{Mn}_y\text{O}_2$ Lattice at Deep Charge Irrespective of Nickel Content in Lithium-Ion Batteries. *J. Am. Chem. Soc.* **2019**, *141*, 5097–5101.

(35) Ryu, H.-H.; Park, K.-J.; Yoon, C. S.; Sun, Y.-K. Capacity Fading of Ni-Rich $\text{Li}[\text{Ni}_x\text{Co}_y\text{Mn}_{1-x-y}\text{O}_2]$ ($0.6 \leq x \leq 0.95$) Cathodes for High-Energy-Density Lithium-Ion Batteries: Bulk or Surface Degradation? *Chem. Mater.* **2018**, *30*, 1155–1163.

(36) Yoon, C. S.; Jun, D.-W.; Myung, S.-T.; Sun, Y.-K. Structural Stability of LiNiO_2 Cycled above 4.2 V. *ACS Energy Lett.* **2017**, *2*, 1150–1155.

(37) Kondrakov, A. O.; Geßwein, H.; Galdina, K.; De Biasi, L.; Meded, V.; Filatova, E. O.; Schumacher, G.; Wenzel, W.; Hartmann, P.; Brezesinski, T.; Janek, J. Charge-Transfer-Induced Lattice Collapse in Ni-Rich NCM Cathode Materials during Delithiation. *J. Phys. Chem. C* **2017**, *121*, 24381–24388.

(38) Li, J.; Harlow, J.; Stakheiko, N.; Zhang, N.; Paulsen, J.; Dahn, J. Dependence of Cell Failure on Cut-Off Voltage Ranges and Observation of Kinetic Hindrance in $\text{LiNi}_{0.8}\text{Co}_{0.15}\text{Al}_{0.05}\text{O}_2$. *J. Electrochem. Soc.* **2018**, *165*, A2682–A2695.

(39) Hildebrand, S.; Vollmer, C.; Winter, M.; Schappacher, F. M. Al_2O_3 , SiO_2 and TiO_2 as Coatings for Safer $\text{LiNi}_{0.8}\text{Co}_{0.15}\text{Al}_{0.05}\text{O}_2$ Cathodes: Electrochemical Performance and Thermal Analysis by Accelerating Rate Calorimetry. *J. Electrochem. Soc.* **2017**, *164* (9), A2190–A2198.

(40) Woo, S.-U.; Yoon, C. S.; Amine, K.; Belharouak, I.; Sun, Y.-K. Significant Improvement of Electrochemical Performance of AlF_3 -Coated $\text{Li}[\text{Ni}_{0.8}\text{Co}_{0.1}\text{Mn}_{0.1}\text{O}_2]$ Cathode Materials. *J. Electrochem. Soc.* **2007**, *154*, A1005–A1009.

(41) Yan, P.; Zheng, J.; Liu, J.; Wang, B.; Cheng, X.; Zhang, Y.; Sun, X.; Wang, C.; Zhang, J. G. Tailoring Grain Boundary Structures and Chemistry of Ni-Rich Layered Cathodes for Enhanced Cycle Stability of Lithium-Ion Batteries. *Nat. Energy* **2018**, *3*, 600–605.

(42) Cheng, X.; Zheng, J.; Lu, J.; Li, Y.; Yan, P.; Zhang, Y. Realizing Superior Cycling Stability of Ni-Rich Layered Cathode by Combination of Grain Boundary Engineering and Surface Coating. *Nano Energy* **2019**, *62*, 30–37.

(43) Lee, S.-W.; Kim, M.-S.; Jeong, J. H.; Kim, D.-H.; Chung, K. Y.; Roh, K. C.; Kim, K.-B. Li_3PO_4 Surface Coating on Ni-Rich $\text{LiNi}_{0.6}\text{Co}_{0.3}\text{Mn}_{0.2}\text{O}_2$ by a Citric Acid Assisted Sol-Gel Method: Improved Thermal Stability and High-Voltage Performance. *J. Power Sources* **2017**, *360*, 206–214.

(44) Chen, Z.; Kim, G. T.; Guang, Y.; Bresser, D.; Diemant, T.; Huang, Y.; Copley, M.; Behm, R. J.; Passerini, S.; Shen, Z. Manganese Phosphate Coated $\text{Li}[\text{Ni}_{0.6}\text{Co}_{0.2}\text{Mn}_{0.2}\text{O}_2]$ Cathode Material: Towards Superior Cycling Stability at Elevated Temperature and High Voltage. *J. Power Sources* **2018**, *402*, 263–271.

(45) Gu, W.; Dong, Q.; Zheng, L.; Liu, Y.; Mao, Y.; Zhao, Y.; Duan, W.; Lin, H.; Shen, Y.; Chen, L. Ambient Air Stable Ni-Rich Layered Oxides Enabled by Hydrophobic Self-Assembled Monolayer. *ACS Appl. Mater. Interfaces* **2020**, *12*, 1937–1943.

(46) Kang, T.; Wang, Y.; Guo, F.; Liu, C.; Zhao, J.; Yang, J.; Lin, H.; Qiu, Y.; Shen, Y.; Lu, W.; Chen, L. Self-Assembled Monolayer Enables Slurry-Coating of Li Anode. *ACS Cent. Sci.* **2019**, *5*, 468–476.

(47) Zeng, L.; Shi, K.; Qiu, B.; Liang, H.; Li, J.; Zhao, W.; Li, S.; Zhang, W.; Liu, Z.; Liu, Q. Hydrophobic Surface Coating against Chemical Environmental Instability for Ni-Rich Layered Oxide Cathode Materials. *Chem. Eng. J.* **2022**, *437*, No. 135276.

(48) Wagner, N. P.; Tolchard, J. R.; Tron, A.; Pollen, H. N.; Gaertner, H.; Vullum, P. E. Improved Cyclability of Nickel-Rich Layered Oxides. *MRS Adv.* **2020**, *5*, 1433–1440.

(49) Pollen, H. N.; Tolchard, J. R.; Svensson, A. M.; Wagner, N. P. A Single-Pot Co-Precipitation Synthesis Route for Ni-Rich Layered Oxide Materials with High Cycling Stability. *ChemElectroChem* **2022**, *9*, No. e202200859.

(50) Quiñones, R.; Shoup, D.; Behnke, G.; Peck, C.; Agarwal, S.; Gupta, R. K.; Fagan, J. W.; Mueller, K. T.; Iulucci, R. J.; Wang, Q. Study of Perfluorophosphonic Acid Surface Modifications on Zinc Oxide Nanoparticles. *Materials* **2017**, *10*, 1363.

(51) Chen, D.; Wu, H. K. Y.; Naderi-Gohar, S.; Wu, Y.; Huang, Y.; Nie, H.-Y. An Extremely Rapid Dip-Coating Method for Self-Assembly of Octadecylphosphonic Acid and Its Thermal Stability on an Aluminum Film. *J. Mater. Chem. C* **2014**, *2*, 9941–9948.

(52) Ye, H.-J.; Shao, W.-Z.; Zhen, L. Tetradecylphosphonic Acid Modified BaTiO_3 Nanoparticles and Its Nanocomposite. *Colloids Surf., A* **2013**, *427*, 19–25.

(53) Wan, X.; Lieberman, I.; Asyuda, A.; Resch, S.; Seim, H.; Kirsch, P.; Zharnikov, M. Thermal Stability of Phosphonic Acid Self-Assembled Monolayers on Alumina Substrates. *J. Phys. Chem. C* **2020**, *124*, 2531–2542.

(54) Liu, H.; Naylor, A. J.; Menon, A. S.; Brant, W. R.; Edström, K.; Younesi, R. Understanding the Roles of Tris(trimethylsilyl) Phosphite (TMSPi) in $\text{LiNi}_{0.8}\text{Mn}_{0.1}\text{Co}_{0.1}\text{O}_2$ (NMC811)/Silicon-Graphite (Si-Gr) Lithium-Ion Batteries. *Adv. Mater. Interfaces* **2020**, *7*, No. 2000277.

(55) Wang, T.; Ren, K.; Xiao, W.; Dong, W.; Qiao, H.; Duan, A.; Pan, H.; Yang, Y.; Wang, H. Tuning the Li/Ni Disorder of the NMC811 Cathode by Thermally Driven Competition Between Lattice Ordering and Structure Decomposition. *J. Phys. Chem. C* **2020**, *124*, S600–S607.

(56) Gieu, J. B.; Winkler, V.; Courrèges, C.; El Ouatani, L.; Tessier, C.; Martinez, H. New Insights into the Characterization of the Electrode/Electrolyte Interfaces within $\text{LiMn}_2\text{O}_4/\text{Li}_4\text{Ti}_3\text{O}_{12}$ Cells, by X-Ray Photoelectron Spectroscopy, Scanning Auger Microscopy and Time-of-Flight Secondary ion mass spectrometry. *J. Mater. Chem. A* **2017**, *5*, 15315–15325.

(57) Gauthier, N.; Courrèges, C.; Demeaux, J.; Tessier, C.; Martinez, H. Probing the In-Depth Distribution of Organic/Inorganic Molecular Species within the SEI of LTO/NMC and LTO/LMO Batteries: A Complementary ToF-SIMS and XPS Study. *Appl. Surf. Sci.* **2020**, *501*, No. 144266.

(58) Malmgren, S.; Ciosek, K.; Hahlin, M.; Gustafsson, T.; Gorgoi, M.; Rensmo, H.; Edström, K. Comparing Anode and Cathode Electrode/Electrolyte Interface Composition and Morphology Using Soft and Hard X-Ray Photoelectron Spectroscopy. *Electrochim. Acta* **2013**, *97*, 23–32.

(59) Huang, C.; Sun, T.; Hulicova-Jurcakova, D. Wide Electrochemical Window of Supercapacitors from Coffee Bean-Derived Phosphorus-Rich Carbons. *ChemSusChem* **2013**, *6*, 2330–2339.

(60) Scientific, T. F. Table of Elements: X-ray Photoelectron Spectroscopy of Atomic Elements, 2023. <https://www.thermofisher.com/no/en/home/materials-science/learning-center/periodic-table.html>.

(61) Zhang, L.; Gao, Y.; Xu, Y.; Liu, J. Different Performances and Mechanisms of Phosphate Adsorption onto Metal Oxides and Metal Hydroxides: A Comparative Study. *J. Chem. Technol. Biotechnol.* **2016**, *91*, 1232–1239.

(62) Shih, P. Y.; Yung, S. W.; Chin, T. S. FTIR and XPS Studies of $\text{P}_2\text{O}_5\text{-Na}_2\text{O-CuO}$ Glasses. *J. Non-Cryst. Solids* **1999**, *244*, 211–222.

(63) Sydoruk, V.; Poddubnaya, O. I.; Tsyba, M. M.; Zakutevskyy, O.; Khyzhun, O.; Khalameida, S.; Puziy, A. M. Photocatalytic Degradation of Dyes Using Phosphorus-Containing Activated Carbons. *Appl. Surf. Sci.* **2021**, *535*, No. 147667.

(64) Biesinger, M. X-ray Photoelectron Spectroscopy (XPS) Reference, 2023. <http://www.xpsfitting.com/>.

(65) Ohzuku, T.; Ueda, A.; Yamamoto, N. Zero-Strain Insertion Material of $\text{Li}[\text{Li}_{1/3}\text{Ti}_{5/3}\text{O}_4]$ for Rechargeable Lithium Cells. *J. Electrochem. Soc.* **1995**, *142*, 1431–1435.

(66) Li, W.; Reimers, J. N.; Dahn, J. R. In Situ X-Ray Diffraction and Electrochemical Studies of $\text{Li}_{1-x}\text{NiO}_2$. *Solid State Ionics* **1993**, *67*, 123–130.

(67) Lin, Q.; Guan, W.; Meng, J.; Huang, W.; Wei, X.; Zeng, Y.; Li, J.; Zhang, Z. A New Insight into Continuous Performance Decay Mechanism of Ni-Rich Layered Oxide Cathode for High Energy Lithium Ion Batteries. *Nano Energy* **2018**, *54*, 313–321.

(68) Yoon, C. S.; Ryu, H.-H.; Park, G.-T.; Kim, J.-H.; Kim, K.-H.; Sun, Y.-K. Extracting Maximum Capacity from Ni-Rich $\text{Li}[\text{Ni}_{0.95}\text{Co}_{0.025}\text{Mn}_{0.025}]\text{O}_2$ Cathodes for High-Energy-Density Lithium-Ion Batteries. *J. Mater. Chem. A* **2018**, *6*, 4126–4132.

(69) Park, K.-J.; Hwang, J.-Y.; Ryu, H.-H.; Maglia, F.; Kim, S.-J.; Lamp, P.; Yoon, C. S.; Sun, Y. K. Degradation Mechanism of Ni-Enriched NCA Cathode for Lithium Batteries: Are Microcracks Really Critical? *ACS Energy Lett.* **2019**, *4*, 1394–1400.

(70) Li, J.; Liu, H.; Xia, J.; Cameron, A. R.; Nie, M.; Botton, G. A.; Dahn, J. R. The Impact of Electrolyte Additives and Upper Cut-off Voltage on the Formation of a Rocksalt Surface Layer in $\text{LiNi}_{0.8}\text{Mn}_{0.1}\text{Co}_{0.1}\text{O}_2$ Electrodes. *J. Electrochem. Soc.* **2017**, *164*, A655–A665.